Near-Surface Air Temperature Measurements: Contribution to the Overall Uncertainty due to Wind Speed and Relative Humidity

Original
Near-Surface Air Temperature Measurements: Contribution to the Overall Uncertainty due to Wind Speed and Relative Humidity / Aranda, N.G., Bottacin, A., Coppa, G., Musacchio, C., Merlone, A.. - In: METEOROLOGICAL APPLICATIONS. - ISSN 1350-4827. - 33:4(2026). [10.1002/met.70218]

Availability:
This version is available at: 11696/90059 since: 2026-07-23T12:12:02Z

Publisher:
Wiley

Published
DOI:10.1002/met.70218

Meteorological Applications

RMetS Royal Meteorological Society

RESEARCH ARTICLE OPEN ACCESS

Near-Surface Air Temperature Measurements: Contribution to the Overall Uncertainty due to Wind Speed and Relative Humidity

Natali Giselle Aranda | Alberto Bottacin | Graziano Coppa | Chiara Musacchio | Andrea Merlone

National Metrology Institute of Italy, INRiM, Turin, Italy

Correspondence: Natali Giselle Aranda (n.aranda@inrim.it)

Received: 16 September 2025 | **Revised:** 12 June 2026 | **Accepted:** 25 June 2026

Keywords: ground-based stations | meteorological and climatological observations | near-surface air temperature measurements | uncertainty

ABSTRACT

In the context of global warming, ensuring the comparability and traceability of air temperature measurements is essential for accurately characterising climate change. However, quantifying the environmental effects under real measurement conditions is still a key challenge for the meteorological community. This study addresses this issue by improving the understanding of air temperature observation uncertainties from ground-based stations. Data from six identical thermometers at 1.60 m and 2.10 m, protected with the same ventilated solar shield and connected to the same datalogger, were analysed during summer and winter. Air temperature difference (ΔT) was calculated as the difference between the readings of each thermometer and the mean, while wind speed and relative humidity were considered quantities of influence. The analysis shows that ΔT depends on season, sensor height, wind speed and relative humidity. During winter nights, ΔT reflects the influence of fog and condensation, intensified by low wind speed. ΔT also exhibits a clear diurnal cycle, indicating the presence of a solar heating effect. The uncertainty of ΔT was then calculated across different ranges of air temperature, wind speed, and relative humidity, obtaining values between 0.03°C and 0.12°C for both thermometer heights. For instance, during a summer daytime case, the air temperature at 1.60 m reached 32.25°C with an uncertainty due to wind speed and relative humidity equal to 0.06°C. Overall, the results show that the uncertainty decreases as wind speed increases, independently of seasonal conditions and thermometer height. This work provides uncertainty values derived from real environmental conditions that can be incorporated in the environmental effects component of the overall measurement uncertainty, in line with the World Meteorological Organisation requirements. These results also support the evaluation of uncertainty budgets for climate reference stations, providing uncertainty values applicable to other stations with similar measurement setups.

1 | Introduction

Surface air temperature is defined as an Essential Climate Variable (ECV) for the study of climate change (WMO GCOS-138 2010a; WMO GCOS-143 2010b; Bojinski et al. 2014). This variable, crucial for decision-makers, has the mission to present global availability and guarantee the high quality of its observations and products. In this context, there is an increasing demand for traceable and reliable air temperature observations. As an ECV, surface air temperature measurements must be traceable to standards of the International System of Units, SI. Furthermore, all the sources of uncertainty must be identified, and the measurement results must be expressed with their corresponding expanded uncertainty (Merlone et al. 2024).

The requirements for ECV measurements are described in GCOS-245 (WMO GCOS-245 2025), which provides recommendations for a sustained and fit Global Climate Observing

System. Regarding the uncertainty requirement for near surface air temperature measurements, the breakthrough threshold required is 0.5 K, including all the uncertainty contributions. According to the definitions provided in the Guide to the expression of uncertainty in measurement or GUM (JCGM 2008), uncertainties are classified into two types: Type A, obtained from statistical methods, and Type B, which are non-statistical, such as those based on instrument characteristics.

Currently, air thermometers from ground-based stations are calibrated in laboratories. However, this procedure does not consider the real measurement conditions, in which environmental variables such as wind or solar radiation introduce errors and contribute to the overall uncertainty. In fact, the GUM requires that all contributions of uncertainty, including the environmental ones, be included in the uncertainty budget. And works like Woolliams et al. (2025) highlight the importance of incorporating auxiliary information as environmental conditions in the uncertainty model.

A thermometer exposed freely in an open space can absorb considerable radiation, generating differences between the temperature reading and the true air temperature. To minimise the radiation effect, the World Meteorological Organisation (WMO) recommends the use of shiny thermometers (that reflect rather than absorb radiation), with small diameters (they are effectively cooled by the air) (Çengal and Ghajar 2015; de Podesta et al. 2018). However, even when such precautions are taken, reflected radiation can still influence measurements. Musacchio et al. (2019, 2021), working with temperature measurements in snow conditions, have pointed out that the reflected radiation can cause extra warming near the sensors, affecting the heat transfer and thus increasing the temperature values. It was observed that sensors above a snow-covered surface, due to the larger amount of radiation reflected, present higher values of air temperature.

In the presence of precipitation, evaporation cools down the air temperature values. The water temperature is normally colder and removes further heat from the thermometers' shields, resulting in errors in the air temperature reading due to the lower values of temperature near the sensors. In this sense, the work of Nielsen et al. (2024) quantifies the influence of rain on the readings of temperature sensors, using radiation screens of different types. The experiment considered different rates of rain intensity. In the case of low rain, "the evaporation of water droplets from the screen plates decreases the temperature of the microclimate inside the screen, while the evaporation from the sensor could directly decrease its temperature". The test has shown that the average error is less significant for ventilated air thermometers, being (-1.1 ± 0.2) K, when the rainfall intensity is 0.6 L min^{-1}.

The works of Harrison have focused on the effect of wind speed on air temperature measurements. First, he has compared the temperature measurements made in the Stevenson screen and outside (R. G. Harrison 2010). The experiment showed that the largest temperature differences generally were registered at low wind speed values. In these conditions and during nights with clear skies, the screen also became cooler than its surrounding air due to the radiative cooling. A few years later, Harrison and Burt (2021) evaluated the uncertainty contribution due to the ventilation effect on air temperature measurements. Using an aspirated thermometer as a reference, the study showed that radiation exchange and time response are the most important contributors to the highest absolute differences. Furthermore, it was observed that the radiation effect increases when the wind speed is lower than 1 m s^{-1}.

Hence, the principal meteorological variables that affect the air temperature measurements are solar radiation, wind speed, humidity, and precipitation (Thorne et al. 2016). Errors in temperature measurements are reduced on days with wind blowing and reduced solar radiation. Conversely, on sunny days and low or absence of wind, the influences on temperature readings would be high. Regarding humidity, high humidity can cause condensation on the thermometer surface, and the thermometer readings cannot reflect the current air temperature. In the presence of precipitation, the evaporation will cool the sensor. Moreover, precipitation, drizzle, and fog conditions might generate condensation on the solar shield that protects the thermometer from the direct solar radiation, raising the differences between the measured temperature and the true air temperature.

Although the influence of atmospheric parameters and physical processes on air temperature measurements has been studied, not all the components have been quantified (e.g., height of the sensor from the ground, evaporation of precipitation on screens, wind and solar radiation effects on measurements). Moreover, their interactions are still poorly understood. Therefore, the goal of this work is to further investigate the air temperature observation uncertainties from ground-based stations. Metrological and meteorological communities, supported by the WMO, are working on definitions and designs of Climatological Reference Stations (CRSs), aiming to detect climate trends. In this regard, the CRSs propose the adoption of standardised prescription of technical setup, measurement procedures and uncertainty evaluation, in order to improve data comparability in space and time, for a more robust understanding of climate evolution locally and globally (GCOS 2021; Merlone et al. 2024). Currently, quantifying the uncertainty of air temperature measurements under real measurement conditions is a major challenge for the meteorological community and is essential for the Measurement Quality Classification Scheme (WMO 2024a, Annex 1.G) and for the CRSs. For this, data from a system of six identical thermometers, installed at two heights in an open field, are analysed. The differences between the readings of each thermometer and the mean of the six were calculated and called ΔT. Wind speed (WS) and relative humidity (RH) measurements are used as quantities of influence (Merlone et al. 2024), and ΔT was evaluated for different combinations of air temperature ranges and associated quantities of influence. The analysis is completed with the quantification and evaluation of the corresponding uncertainty, identified as the air temperature uncertainty due to WS and RH. Thus, this work addresses the requirement of the meteorological and climatological community by providing an uncertainty evaluation of air temperature measurements under real measurement conditions.

2 | Methodology

2.1 | Data and Methodology

Data from six Pt100 thermometers, one hygrometer, and one ultrasonic wind sensor were evaluated. The sensors were installed and operated for almost 2 years at the National Metrology Institute of Italy, INRiM, in Turin (Figure 1). The topography influences the climatological conditions of the studied area. Turin is bordered by the Alps mountain in the west and hills in the east, and the experimental field is 3 km from the Po River and 1 km from the Sangone Torrent. Hence, the city is characterised by high humidity and low winds, with some Foehn events (Cassardo et al. 2002; Fratianni et al. 2009).

The temperature sensors were installed at different heights: three at 1.60 m from the ground and the other three at 2.10 m. Positioning the thermometers at different heights but at the same spatial location, the uncertainty associated with the distance between instruments is reduced. To avoid possible observational errors, the air temperature was measured by identical thermometers protected from direct solar radiation with the same Young ventilated solar shield. The fan, located in the upper part, extracts air from the bottom of the shield and discharges it above the cover. In this configuration, fresh flow of air coming from below the shield always surrounds the thermometer. Furthermore, the sensors were connected to the same datalogger. Thus, the self-heating does not alter the relative readings among them (Coppa et al. 2021).

Before the installation, the thermometers were calibrated against reference standards at the INRiM laboratories, guaranteeing the reliability of the data. The thermometers were calibrated in a climatic chamber at eight temperature points (−15, −5, 0, 5, 15, 25, 35, 40)°C, with the same datalogger and setup used in the experiment, reading their resistance and then producing a Callendar-van Dusen (CVD) calibration curve. The expanded uncertainty reported in the calibration certificate is 0.04°C, with a level of confidence of 95% ($k = 2$), which corresponds to the highest uncertainty obtained. This uncertainty represents the total uncertainty of the calibration, considering calibration uncertainty of the references, repeatability, homogeneity and stability of the chamber, and calibration curve interpolation.

The wind data was recorded by a Gill WindSonic anemometer. The estimated uncertainty is provided by the manufacturer and is ±1% at 1.2 m s^{-1}. The hygrometer, an ETM-30 by Lombard & Marozzini, was protected with a multiplate solar radiation shield. The calibration by the manufacturer is also assumed, with a declared uncertainty of 0.5%. All the instruments were connected to the same datalogger, operated from 19 February 2020 to 15 July 2020 and from 15 July 2021 to 10 March 2022. The data were simultaneously recorded every 10 s.

The air temperature difference between each thermometer and the mean temperature of the six sensors, ΔT_i, is calculated:

$$\Delta T_i = T_i - \frac{1}{6}\sum_{i=1}^{6} T_i \tag{1}$$

where T_i is the temperature recorded by each thermometer. In this regard, relative measurements allow to cancel some uncertainty sources from the total budget. There is bibliographic evidence supporting the technique of working with relative

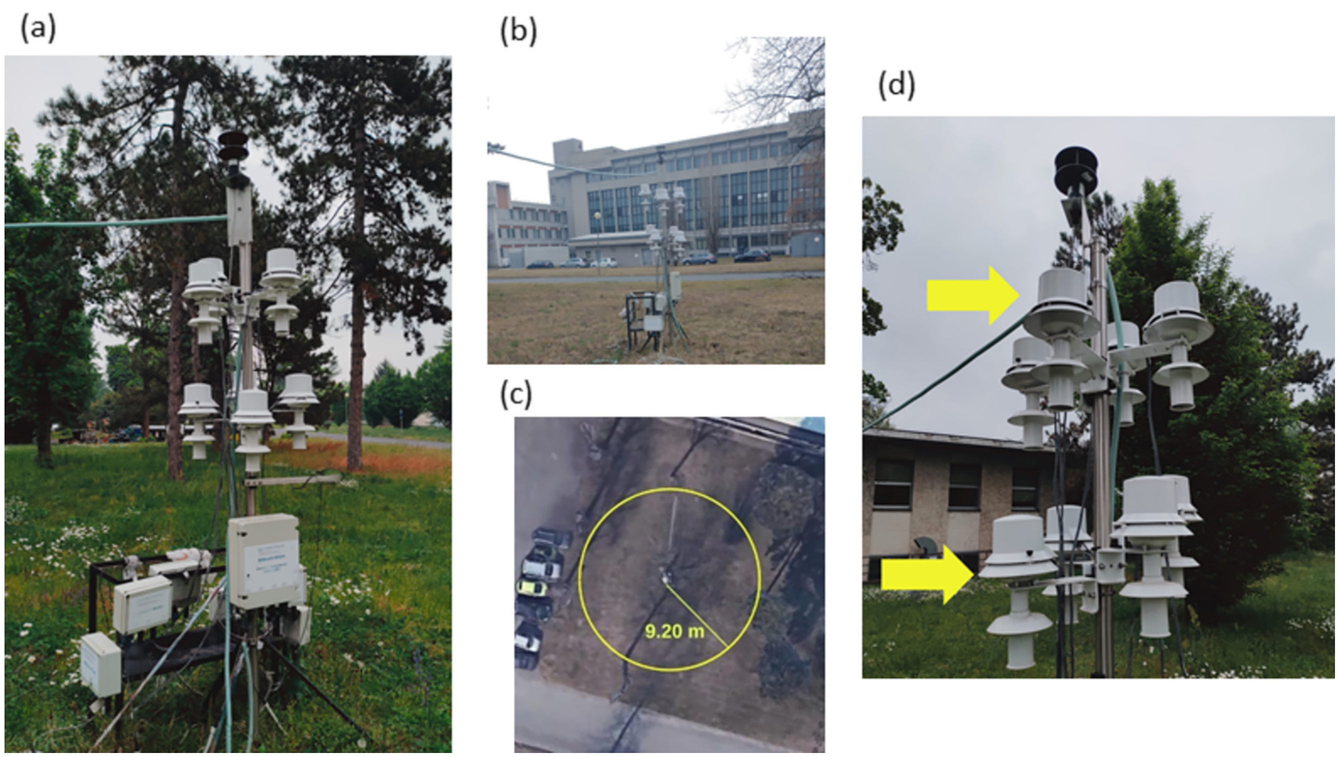

FIGURE 1 | Photographs illustrating the siting and exposure of the meteorological sensors at the INRiM field: (a) eastward view, (b) southward view, and (c) Google Earth image of the site. The measurements presented in this study correspond to the thermometers indicated by the yellow arrow in panel (d).

measurements to cancel some contributions of uncertainty, when all the instruments are the same model, calibrated in the same environment, and read by the same datalogger (Dahl et al. 2003; Merlone et al. 2019; Musacchio et al. 2021; Coppa et al. 2021, 2024). Under these conditions, the uncertainty sources that have been eliminated from the overall budget are: shield characteristics, sensor self-heating, datalogger contribution, instrument maintenance and surface characteristics. All the thermometers had identical solar shields, and any potential error caused by the screen was shared by all the sensors and cancelled out during the computation of ΔT. Moreover, since all the thermometers were identical and powered by the same datalogger, the self-heating did not alter the relative readings, and the uncertainty introduced by the conversion of the resistance to temperature was compensated. Regarding the datalogger contribution, as noted by Coppa et al. (2021), "Modern temperature resistors (such as Pt100 used in this study) measure the resistance of a platinum wire run by an electric current, which is then digitalized, converted into temperature and stored in a datalogger. This process introduces other uncertainties, related to the electronics, the resolution and the accuracy of the resistance measurement." In this work, as Coppa et al. (2021), all the thermometers were read using the same datalogger during both field experiment and laboratory calibration, so the uncertainty introduced by the datalogger is compensated in the relative analysis. The maintenance contribution is considered null since the thermometers were calibrated and maintained with the same methodology. Concerning the surface features, since changes in surface reflectivity affect the measurements, during the study period, the grass was kept short and without any new obstacles that could introduce shadows.

After a visual inspection of the data, it was observed that the behaviour of ΔT varies according to the season. Thus, the present paper analyses the data corresponding to the summer and winter periods. Due to the high temporal resolution of the dataset and to reduce the risk of analysing ΔT more related to the response time of the thermometers than environmental factors, a data quality check was made. This control only considers observations in which the variations between successive temperature values (from the mean temperature) are less than |0.04|°C, that is 61.1% of the summer data and 58.8% of the winter period. The analysis is complemented with the evaluation of uncertainties of ΔT, following the guide in metrology GUM (JCGM 2008). The uncertainty analysis is described in the next Section 2.2, where statistical uncertainties (Type A) and uncertainties due to calibration certificates and instrumental drift (Type B) are identified.

2.2 | Uncertainty Budget

Due to the significant importance of reference measurements in the study of climate change, their uncertainty must be rigorously quantified. Knowing the uncertainty of air temperature measurements will increase confidence in the assessment of global warming, improve data comparability, and provide a more robust understanding of climate evolution. The uncertainty of ΔT is evaluated using Equation (1) and the Law of Propagation of Uncertainty (LPU) (JCGM 2008; 2012). To simplify the analysis, the equation is focused on one thermometer. Thus, the combined uncertainty for a thermometer 1, $u_c(\Delta T_1)$, is:

$$u_c{}^2(\Delta T_1) = \left(\frac{\partial \Delta T_1}{\partial T_1}\right)^2 u^2(T_1) + \left(\frac{\partial \Delta T_1}{\partial T_i}\right)^2 \sum_{i=1}^{6} u^2(T_i) - \frac{\partial \Delta T_1}{\partial T_1}\frac{\partial \Delta T_1}{\partial T_i} cov\left(T_1, \sum_{i=1}^{6} T_i\right) \quad (2)$$

Since the thermometers are of the same type and calibrated using the same reference system, it is possible to assume that $\sum_{i=1}^{6} u^2(T_i) \approx 6u^2(T_1)$. Moreover, $\frac{\partial \Delta T_1}{\partial T_1}$ is 1 and $\frac{\partial \Delta T_1}{\partial T_i}$ is $\frac{-1}{6}$. Additionally, each thermometer was connected to its own electronics and analogue digital converters (ADCs), which sent the air temperature readings to a common datalogger. Thanks to this configuration, the only uncertainty that affects the covariance of T_1 with itself is the calibration uncertainty, that is $u_{cal}(T_1)$. Then, Equation (2) is written as:

$$u_c{}^2(\Delta T_1) = \frac{7}{6}u^2(T_1) - \frac{1}{3}u_{cal}^2(T_1) \quad (3)$$

The uncertainty contributions of the evaluated thermometer are the calibration uncertainty, $u_{cal}(T_1)$, the dispersion of the relative measurements, $u_{disp}(T_1)$, and the thermometer drift, $u_{drift}(T_1)$:

$$u^2(T_1) = u_{cal}^2(T_1) + u_{disp}^2(T_1) + u_{drift}^2(T_1) \quad (4)$$

Regarding the calibration certificate, with $\nu \approx \infty$ degrees of freedom and a t-factor $t_{95}(\infty) = 1.96$, the uncertainty contribution due to the instrument is calculated as:

$$u_{cal}(T_1) = \frac{U_{cal}(T)}{1.96} = 0.02^{\circ}\mathrm{C} \quad (5)$$

The dispersion contribution is calculated based on the air temperature differences, using the pseudo standard deviation, *Sps*, defined as the interquartile range (IQR) divided by 1.349. IQR is the difference between the first and the third quartile, representing the distance covered by the middle half of the distribution. The value of 1.349 represents the IQR for a Gaussian distribution. *Sps* is recommended when the sample is large and/or when the nature of the work is "highly exploratory" (Lanzante 1996). Moreover, *Sps* is a robust and nonparametric statistic, much less affected by the outliers. Therefore, it is recommended for this study.

$$u_{disp}(T_1) = Sps(\Delta T_1) = \frac{\mathrm{IQR}(\Delta T_1)}{1.349} \quad (6)$$

The instrumental drift reflects possible changes in the measurement since the last calibration. To evaluate this contribution, the thermometers were recalibrated using the same setup and reference system as the previous calibration. The new and the old calibration curves are compared using as input nominal resistance values within the calibration range. Then, the observed maximum difference for each sensor is considered the uncertainty associated with instrument drift:

$$u_{drift}(T_1) = \frac{c_i - c_{i-1}}{\sqrt{12}} \quad (7)$$

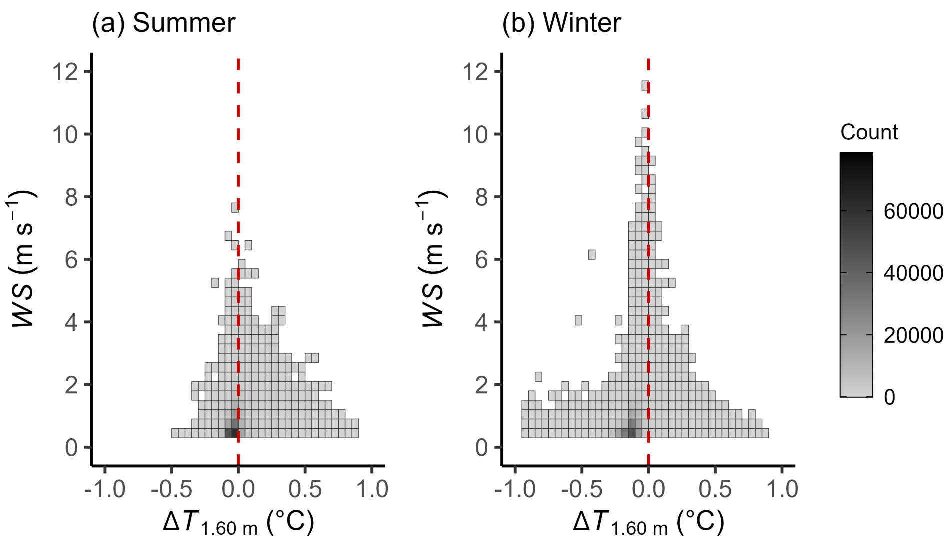

FIGURE 2 | Density plot of *WS* and ΔT observed at 1.60 m, for (a) summer and (b) winter. Each bin represents the number of observations falling within that grid cell, where darker shades indicate higher counts.

where for each nominal value, c_i is the value of the most recent calibration curve and c_{i-1} from the calibration before the thermometer installation. In general, the drift contribution is small, varying between 0.005°C and 0.008°C.

Finally, the combined uncertainty of ΔT_1 depends only on the calibration uncertainty, the dispersion of the relative air temperature measurements and the instrumental drift.

$$u_c{}^2(\Delta T_1) = \frac{7}{6}u_{disp}^2(T_1) + \frac{7}{6}u_{drift}{}^2(T_1) + \frac{5}{6}u_{cal}^2(T_1) \quad (8)$$

The combined uncertainty of ΔT then, represents the uncertainty of air temperature measurements under real measurements conditions. For ground-based stations, according to the Measurement Quality Classification Scheme (WMO 2024a, Annex 1.G), the uncertainty sources for air temperature measurements include the instrument (system) uncertainty and the environment effects, also known as "Associated Quantities of Influence". In this study, the on-site measurements of *WS* and *RH* are used to evaluate the air temperature behaviour across different ranges of these quantities of influence. This methodology allows to investigate how variations in *WS* and *RH* affect the air temperature measurements. Hence, evaluating $u_c(\Delta T)$ for different ranges of air temperature, *WS* and *RH*, it is possible to obtain the air temperature uncertainty due to *WS* and *RH*, that is:

$$u_{WS,RH}(T) \equiv u_c(\Delta T) \quad (9)$$

Section 3.2 aims to exemplify how the results of this work can be integrated in the overall uncertainty of air temperature measurements from ground-based stations, following the Measurement Quality Classification Scheme. For this exercise, the measurements are taken from one sensor at the INRiM field, at 1.60 m. Considering that the calibration of the thermometers had been made using the same datalogger and cables and the datalogger resolution is insignificant with respect to the other contributions (less than 0.001°C), the system uncertainty, $u_{syst}(T)$, only includes the contribution due to the calibration certificate and the instrumental drift. Additionally, an uncertainty due to the influence of *WS* and *RH* is added as part of the environment effects. Finally, the siting measurement uncertainty (type B uncertainty), $u_{siting}(T)$, should be added to get, in combination with the other two uncertainties, the overall temperature measurement uncertainty. In this sense, the combined uncertainty for the air temperature measurements is determined as:

$$u_c{}^2(T) = u_{syst}^2(T) + u_{siting}^2(T) + u_{WS,RH}^2(T) \quad (10)$$

where $u_{syst}^2(T) = u_{cal}^2(T) + u_{drift}^2(T)$ and $u_{siting}(T)$ is obtained from Siting Classifications for Surface Observing Stations on land (WMO 2024a, Annex 1.D). It is important to note that WMO guidelines are continuously revised as new evidence becomes available and as practices evolve within the meteorological community. Recent studies have addressed the siting uncertainty (e.g., Coppa et al. 2021; Garcia Izquierdo et al. 2024) and it may be lower than the values currently reported in the manual. Multiplying $u_c(T)$ by a coverage factor $k = 2$ (95% of confidence level), the expanded uncertainty of air temperature under real measurement conditions, $U(T)$, is obtained.

3 | Results and Discussion

Since all the sensors located at the same height presented similar behaviour, the results shown below correspond to one sensor at 1.60 m and the other at 2.10 m (Figure 1d), both with south exposition. Figure 2 provides evidence of the relationship between ΔT and *WS*. Especially in winter, the lower the *WS*, the greater the temperature differences among the thermometers. Studies have observed that screens with forced ventilation help to reduce temperature biases when the microclimate inside the shield deviates from the surrounding air mass (Burt and de Podesta 2020; Harrison and Burt 2021). However, this figure shows that even with forced ventilation, the temperature differences are more significant when the *WS* is below 2 m s^{-1}.

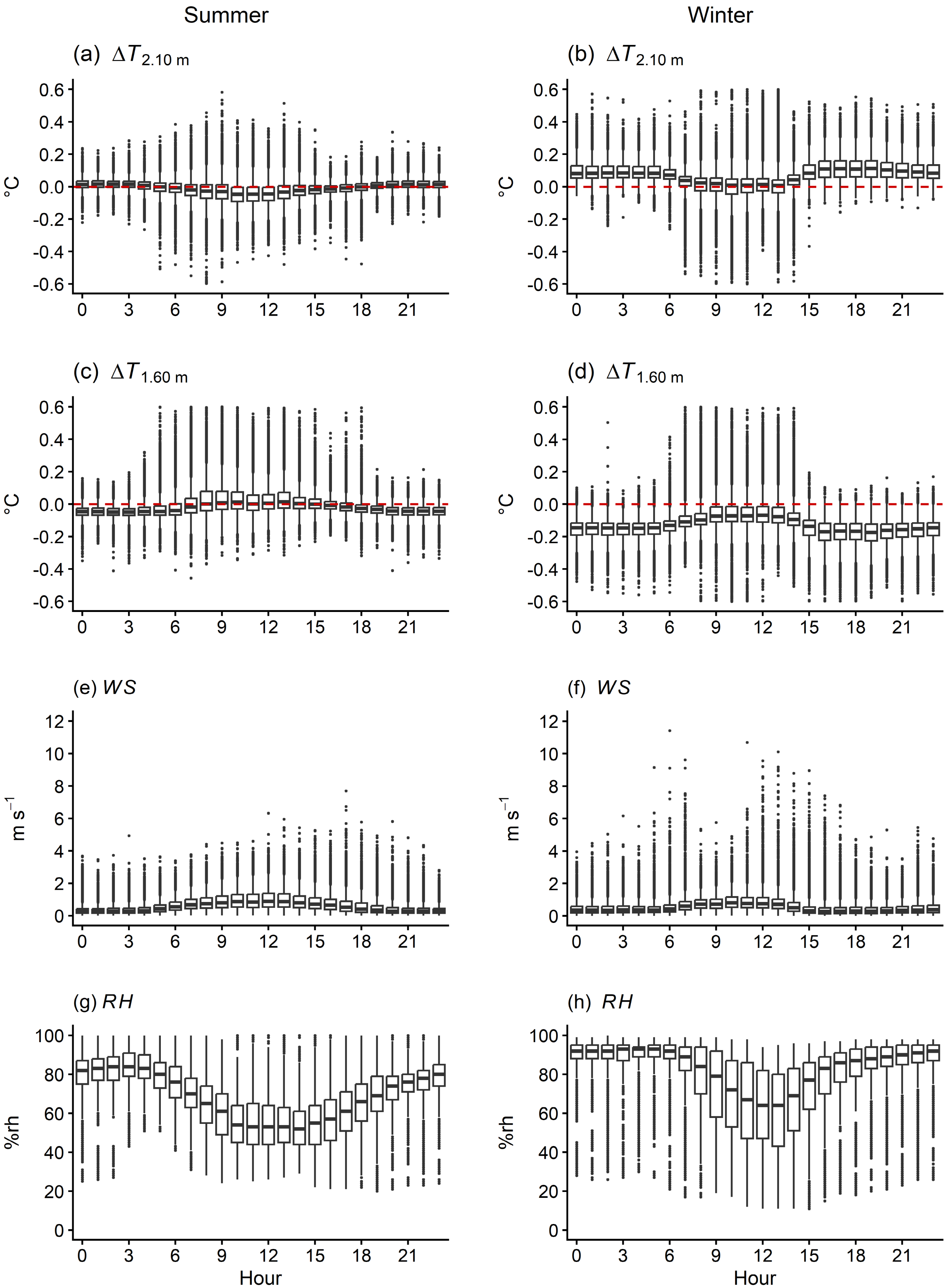

FIGURE 3 | Boxplots of the diurnal evolution of ΔT at 2.10 m (a, b) and 1.60 m (c, d), *WS* (e, f) and *RH* (g, h) for summer and winter, respectively.

TABLE 1 | Mean and median ΔT values and the associated uncertainty components for each air temperature interval (T, defined as the mean of the six thermometers): Dispersion $u_{disp}(T)$, calibration uncertainty $u_{cal}(T)$ and drift $u_{drift}(T)$ for the sensor at 1.60 m and the combined uncertainty of ΔT, $u_c(\Delta T)$.

T (°C)	Mean ΔT (°C)	Median ΔT (°C)	$u_{disp}(T)$ (°C)	$u_{cal}(T)$(°C)	$u_{drift}(T)$ (°C)	$u_c(\Delta T)$ (°C)
$-5 \leq T < 0$	−0.16 (0.09)	−0.15 (0.09)	0.05 (0.06)	0.02 (0.02)	0.005 (0.008)	0.06 (0.07)
$0 \leq T < 5$	−0.15 (0.09)	−0.14 (0.08)	0.06 (0.06)	0.02 (0.02)	0.005 (0.008)	0.07 (0.07)
$5 \leq T < 10$	−0.11 (0.05)	−0.10 (0.04)	0.07 (0.06)	0.02 (0.02)	0.005 (0.008)	0.08 (0.07)
$10 \leq T < 15$	−0.05 (0.02)	−0.07 (0.03)	0.08 (0.06)	0.02 (0.02)	0.005 (0.008)	0.09 (0.07)
$15 \leq T < 20$	−0.05 (0.01)	−0.05 (0.01)	0.03 (0.03)	0.02 (0.02)	0.005 (0.008)	0.04 (0.04)
$20 \leq T < 25$	−0.03 (0.00)	−0.03 (0.00)	0.04 (0.03)	0.02 (0.02)	0.005 (0.008)	0.05 (0.04)
$25 \leq T < 30$	0.01 (−0.02)	−0.01 (−0.02)	0.04 (0.04)	0.02 (0.02)	0.005 (0.008)	0.05 (0.05)
$30 \leq T < 35$	0.04 (−0.04)	0.02 (−0.04)	0.05 (0.05)	0.02 (0.02)	0.005 (0.008)	0.06 (0.06)

Note: Values in brackets correspond to the sensor at 2.10 m.

To investigate the diurnal variability of ΔT, ΔT, WS and RH are plotted by hour of the day and shown in Figure 3. In winter, after mid-afternoon and throughout the night, there is a decoupling between the air temperature at the two heights (Figure 3b,d). During the cold period, radiation fog, where cooling is the main physical mechanism of fog formation, is usually observed in the study area. Fog induces condensation on the surface of the screens, which increases the temperature difference among the thermometers (Nakamura and Mahrt 2005; R. G. Harrison 2015; WMO 2024a). During winter nights, RH frequently reaches values around 90%rh (Figure 3h), suggesting that conditions are generally favourable for condensation. Additionally, in conditions of calm (< 0.5 m s^{-1}) and light air (0.3–1.5 m s^{-1}) (Figure 3f), the air remains stratified, increasing the difference between the temperature recorded by the sensors at the top and the bottom (Mahrt 1998; Van de Wiel et al. 2017). This decoupling weakens between 9:00 and 13:00, when there is a slight increase in WS, mixing the air between the two levels. In summer, the difference between the temperature values at different heights is still observed, but less pronounced than in winter (Figure 3a,c). During summer nights, the dispersion of the boxplots of ΔT is smaller and increases after sunrise. Due to solar heating, the ground surface is warmer than the air, generating vertical heat flux and, therefore, turbulence (Stull 2012). During the first hours of the day, this turbulence, detected in the series due to the chaotic wind direction values (not shown), amplifies the temperature differences among the thermometers. As a result, the boxplots of ΔT show larger dispersion during these hours.

These observed patterns are because the ground-based observations are performed in the boundary layer, which is the portion of the troposphere strongly influenced by the exchange of momentum, heat, and moisture with the Earth's surface. The surface layer, which is the bottom region of the boundary layer, is where the meteorological instruments of this experiment are located. Figure 3 shows that the sensor at 1.60 m, which is strongly influenced by surface-driven convection, generally observes lower temperatures at night (negative values of ΔT) and higher temperatures during the day (positive values of ΔT). The temperature behaviour at 2.10 m is the opposite. The surface layer becomes stably stratified when the ground is cooler than the air, and the temperature increases with height (Stull 2012). Thus, during the cooling, the sensor at 1.60 m records lower air temperature values, and the other sensor at 2.10 m measures higher air temperature values. On the contrary, in the presence of solar heating, when the ground is warmer than the air, the air temperature values decrease with height. Nevertheless, the difference between the temperature medians at two heights is less than 0.3°C.

Figure 3 indicates a clear diurnal cycle in RH and WS, which is consequently observed in ΔT. Although the study area is characterised by low WS, the wind is slightly stronger during the daytime and weaker at night. This behaviour is fully consistent with previous studies (He et al. 2013; Fajber et al. 2014; Ashkenazy and Yizhaq 2023; Dai 2023). Over land, this diurnal cycle arises from the small heat capacity of the ground: during the day, the surface warms quickly, resulting in convection that promotes convective mixing and enhances near-surface winds; while at night, the surface cools quickly, generating stable conditions that suppress turbulence and reduce WS. Regarding the humidity, it is physically linked to air temperature. As the surface warms during the day, the saturation vapour pressure, which depends directly and exponentially on temperature, increases rapidly, leading to lower RH. After sunset, cooling reduces the saturation vapour pressure, causing RH to rise and often approach saturation (Markowski and Richardson 2011; Stull 2012; Dai 2023). In particular, the high humidity in winter in the study area is associated to the cold temperature and the frequent occurrence of fog.

ΔT was further analysed by grouping the data into air temperature intervals of 5°C. This approach allows to analyse how ΔT behaves across temperature conditions, taking as reference the mean of the six thermometers. The temperature records evaluated in winter vary between −5°C and 15°C, while in summer, between 15°C (inclusive) and 35°C. Table 1 summarises the mean and median of ΔT, with the corresponding uncertainty contributions.

Observing the temperature differences from Table 1, generally in winter, the bottom sensor tends to observe lower temperatures, while the sensor at the top records higher values. The dataset reveals that temperature values lower than 5°C were recorded at night, while temperature records higher than or equal to 30°C were recorded during daytime hours. Hence, this pattern aligns with the diurnal evolution illustrated in Figure 3. To continue analysing the behaviour of the thermometers at different heights, different times of day and seasons, Figures 4 and 5 are shown. To ensure a representative analysis, specific temperature thresholds were selected based on their highest frequency of occurrence during the night (00:00–06:00) and during the afternoon (12:00–18:00). These figures show that during the night, the values of ΔT were observed in the presence of WS lower than 4 m s^{-1} and, in general, high RH values. Despite this, the relative histograms of ΔT are different for both seasons: the stratification of ΔT with height is evident during winter nights (Figure 4). As mentioned before, fog is commonly observed at the INRiM field and condensation on the surface screen can affect the temperature readings, increasing the temperature differences among the thermometers. If low wind or calm conditions are present, the air remains stratified, further increasing the temperature difference between the sensors at the top and bottom. Conversely, on summer nights (Figure 5), although the large dispersion of ΔT is associated with RH between 70 and 90%rh and WS below 1 m s^{-1}, the temperature differences between the sensors at 1.60 m and 2.10 m are less pronounced. On summer nights, condensation on the screen due to fog does not occur and the rate of radiative heat loss from the ground is lower (Garratt 1992; Mahrt 1998; Stull 2012). During summer days, the effect of solar heating is significant and the soil stores more heat during the day, which is then released, slowly, during the

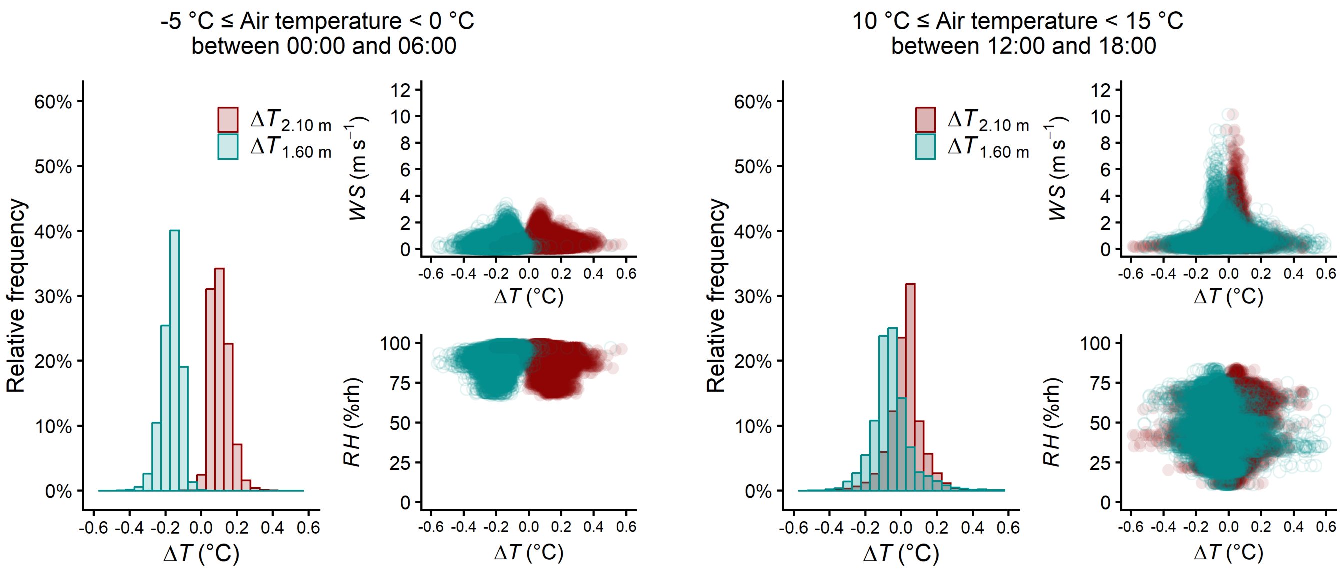

FIGURE 4 | Winter measurements for specific air temperature intervals during night-time (00:00–06:00) and afternoon (12:00–18:00). The image shows the relative histogram of ΔT, and the plots of WS and RH vs. ΔT. Data from the sensor at 1.60 m are shown in red and data from the sensor at 2.10 m, in blue.

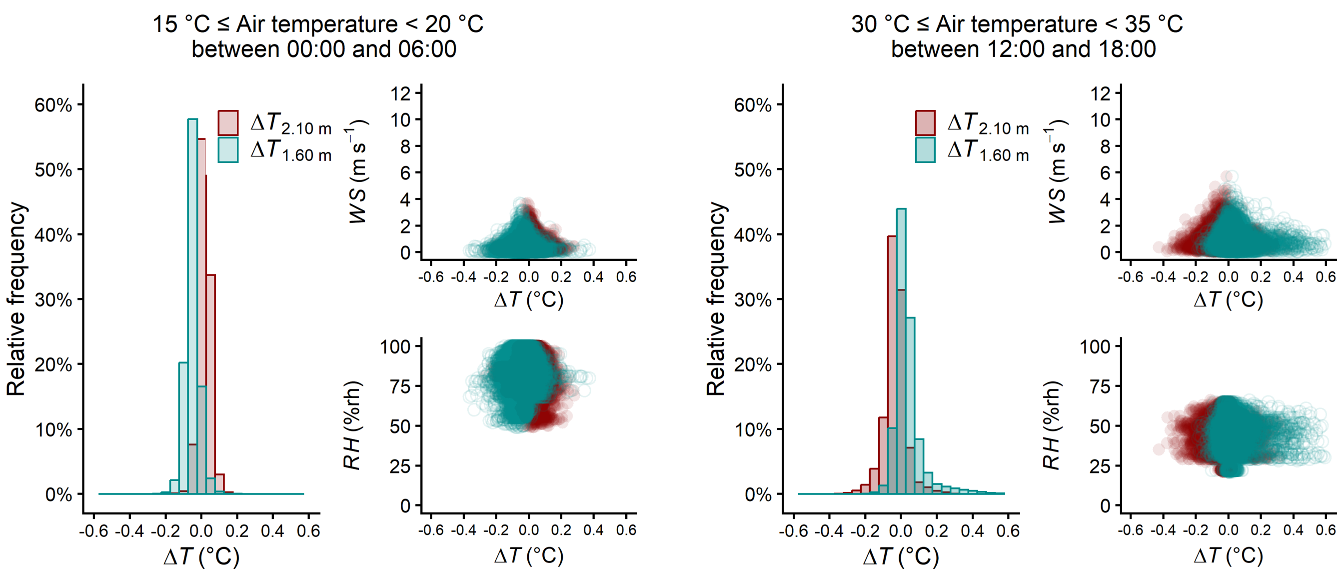

FIGURE 5 | Summer measurements for specific air temperature intervals during night-time (00:00–06:00) and afternoon (12:00–18:00). The image shows the relative histogram of ΔT, and the plots of WS and RH vs. ΔT. Data from the sensor at 1.60 m are shown in red and data from the sensor at 2.10 m, in blue.

night. This upward heat flux counteracts the air stratification, reducing the temperature difference between the two heights.

The measurements recorded in the summer afternoon evidence the influence of solar heating on the dispersion of temperature measurements, where the surface layer becomes superadiabatic; hence, the temperature decreases with height (Mahrt 1998; Stull 2012). This is reflected in the histogram of ΔT (Figure 5), where their values are shifted to the right for the sensor at 1.60 m, observing warmer temperature values. While the histogram of ΔT at 2.10 m is shifted to the left. In contrast, during the winter afternoon, the thermometer at 1.60 m continues to record lower air temperature values than the sensor at 2.10 m, consistent with night-time observations.

In this way, it was possible to relate different environmental phenomena to the behaviour of ΔT. Observing the uncertainty budget in Table 1, the major contribution is the uncertainty due to the measurement dispersion, which is directly related to the real measurement conditions, thus affected by *WS*, *RH*, solar heating during the day and radiative cooling at night. In particular, on winter nights, the dispersion of ΔT reflects the influence of low wind, condensation, and fog. While in summer daytime, the influence of solar heating and *WS*.

3.1 | Relative Humidity and Wind Speed Influences on Air Temperature Measurements

To deepen the analysis and considering the influence of *WS* and *RH* on air temperature measurements, ΔT and its corresponding uncertainty were calculated considering different thresholds of quantities of influence, for the temperature intervals in Table 1. In this regard, the selected ranges allow us to understand the behaviour of the thermometers under different magnitudes of *WS*, *RH* and the associated physical processes.

Figures 2, 4 and 5 show that the lower the *WS*, the higher the temperature differences among thermometers. In particular for values lower than $2\,\mathrm{m\,s^{-1}}$, the dispersion of ΔT is the highest, even in thermometers with artificial ventilation. This result is, in fact, supported by previous studies. Richardson et al. (1999) investigated the flow efficiency of different solar shields, showing that flow efficiency is a nonlinear function of *WS*, with efficiency decreasing as *WS* decreases, especially below $1\,\mathrm{m\,s^{-1}}$. Lin et al. (2001) showed that, for non-aspirated radiation, high ambient *WS* improves the accuracy of air temperature measurements. However, when *WS* is below $4\,\mathrm{m\,s^{-1}}$, the expected measurement accuracy cannot be achieved. The works of Erell et al. (2005) and Harrison and Burt (2021) demonstrate that at low *WS*, radiation effects dominate, causing errors and increasing the uncertainty of air temperature measurements. Nevertheless, as *WS* increases, convective heat transfer reduces (but it does not eliminate) these errors. Mauder et al. (2008) showed that under calm conditions and for thermometers protected by screens with natural ventilation, air temperature errors may exceed 1°C, and at higher *WS* (greater than $5\,\mathrm{m\,s^{-1}}$) they become generally negligible (< 0.2°C).

Regarding *RH*, more than 88% of the measurements recorded at the INRiM field present values higher than 50%rh. Condensation processes are typically associated with high *RH* conditions, becoming more likely when *RH* exceeds approximately 70–80%rh, depending on the environmental conditions (Best 1953; Stull 2012). According to the WMO (WMO 2024a), phenomena such as dew, fog, or precipitation are generally linked to near-saturation conditions. Therefore, under high humidity conditions, different processes that may introduce measurement errors, such as condensation, wetting, or fog deposition, can be expected. Moreover, *RH* provides indirect information about the thermal regime of the air. At higher temperatures, *RH* typically falls within the range of 25–60%rh, whereas values above 70%rh are more commonly observed at lower temperatures or during night-time cooling (Figures 4 and 5). This relationship reflects the thermodynamic dependence of *RH* on temperature and water vapour content.

Hence, based on the observed behaviour of *WS* and *RH* in the dataset, and consistently with previous studies, the thresholds adopted in this study are summarised in Table 2.

As discussed previously, the uncertainty of ΔT includes not only the uncertainty of air temperature due to calibration and drift contributions, but also the additional uncertainty arising when the thermometers operate under real environmental conditions. For this reason, the uncertainty of ΔT is evaluated across different ranges of *WS* and *RH*, in order to quantify the air temperature uncertainty associated with these quantities of influence, that is $u_{WS,RH}(T)$. Figures 6 and 7 present the results of $u_{WS,RH}(T)$ according to the thresholds from Table 2, and for the temperature intervals from Table 1. These intervals are based on the on-site measurements: air temperature was recorded by each sensor at its corresponding height (2.10 m for Figures 6 and 1.60 m for Figure 7), while *WS* and *RH* were obtained from the co-located meteorological instruments. To ensure statistical significance, those intervals with fewer than 82 observations (less than 0.02% of the seasonal data) were excluded from the analysis.

Considering Equations (8) and (9), the highest contribution to $u_{WS,RH}(T)$ is due to the dispersion of the relative temperature measurements, hence, $u_{disp}(T)$, and this uncertainty component reflects the thermometer performance under real environmental conditions. Under fog conditions, low temperature values (lower than 5°C) and WS lower than $1\,\mathrm{m\,s^{-1}}$, $u_{WS,RH}(T)$ is 0.06°C at both measurement heights. For similar temperature and wind conditions but *RH* in the range 75–85%rh, the uncertainty is slightly higher, ranging from 0.07°C to 0.09°C depending on the sensor height. This behaviour may be associated with the fog dissipation when solar radiation starts to warm the ground surface and

TABLE 2 | Ranges of *WS* and *RH* as quantities of influence on air temperature measurements.

WS ($\mathrm{m\,s^{-1}}$)	*RH* (%rh)
$0 \le WS \le 1$	$0 \le RH \le 50$
$1 < WS \le 2$	$50 < RH \le 70$
$2 < WS \le 4$	$70 < RH \le 85$
$WS > 4$	$85 < RH \le 100$

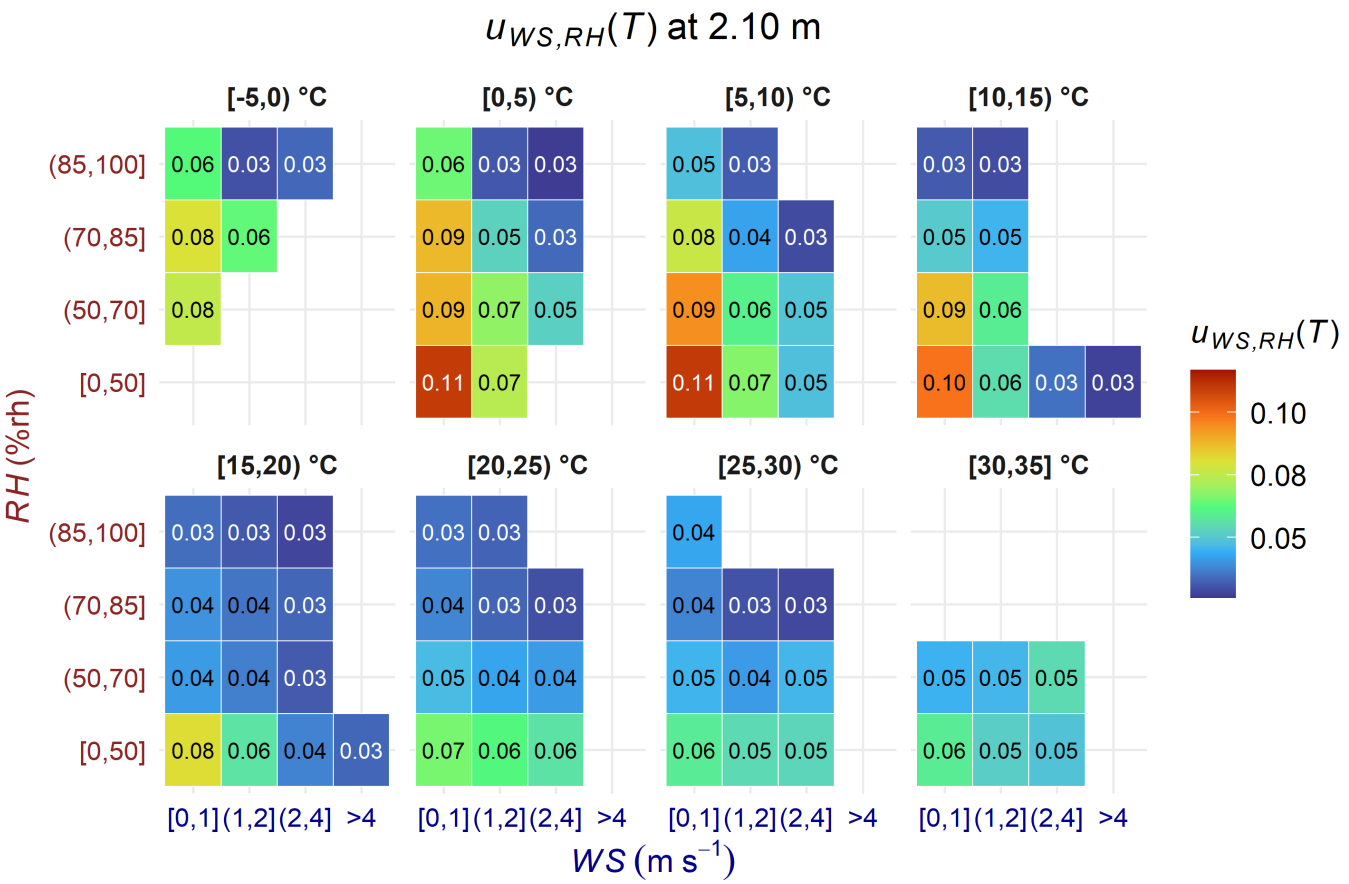

FIGURE 6 | Air temperature uncertainty contribution due to *WS* and *RH*, $u_{WS,RH}(T)$, for the sensor at 2.10 m, evaluated across different combinations of *WS* and *RH* thresholds.

therefore enhances temperature gradients between thermometers, leading to larger measurement dispersion. Comparing the seasons, summer (air temperature values between 15°C, inclusive, and 35°C) presents the smallest uncertainty contribution. However, for both seasons, $u_{WS,RH}(T)$ is high in the presence of low *RH* and low *WS*. Low values of *RH* are associated with large values of solar radiation (Liu et al. 2018), and the temperature conditions in the surface layer are determined by the amount of heat that the ground absorbs (Geiger et al. 2009; Markowski and Richardson 2011). Hence, solar heating plays an important role in the dispersion of the air temperature measurements. Regarding the wind, a consistent pattern is observed, where the uncertainty values decrease as *WS* increases, independently of seasonal conditions and thermometer height. As mentioned before, the wind has the capacity to mix the air surrounding the sensors, decreasing the temperature differences among them. In summer, the decrease of ΔT uncertainties with *WS* is slighter. This is possibly influenced by solar heating, which by convection, reduces the temperature differences among the thermometers and therefore, the temperature dispersion.

3.2 | Case Studies

To complete the evaluation of the uncertainties for air temperature measurements, two case studies are shown: a sunny day in summer (Figure 8) and a foggy day in winter (Figure 9). The data were collected from the sensor pointed out in Figure 1, located at 1.60 m, at the INRiM field. These case studies intend to illustrate how to inform air temperature measurements, including their uncertainties. The weather conditions were verified using meteorological observations from Caselle Station, a meteorological station recognised by the WMO, which is approximately 20 km from the INRiM field. WMO defines the representativeness of an observation as the degree to which it accurately describes the value of the variable needed for a specific purpose; and this representativeness depends on the distance between sites, surface characteristics, topography discontinuities, and the scale of the meteorological phenomena to study (WMO 2024a). As part of the WMO station network, Caselle follows internationally standardised procedures for siting, instrumentation, and quality control, ensuring the reliability and traceability of its measurements. Given the similar altitude, short distance and lack of major topographic barriers between Caselle Station and INRiM, the Caselle observations are representative of the synoptic (e.g., cyclones and fronts) and even mesoscale phenomena (e.g., thunderstorms and fog) that affect the INRiM field experiment, according to the horizontal meteorological scales defined by WMO (WMO-No. 551 1981; WMO 2024b). In the absence of solar radiation observations at the INRiM field, data from Vallere Station were used to corroborate the presence and temporal evolution of solar radiation. These observations were used solely to perform a qualitative analysis of solar radiation during clear-sky and cloudy conditions, rather than to reproduce instant-by-instant

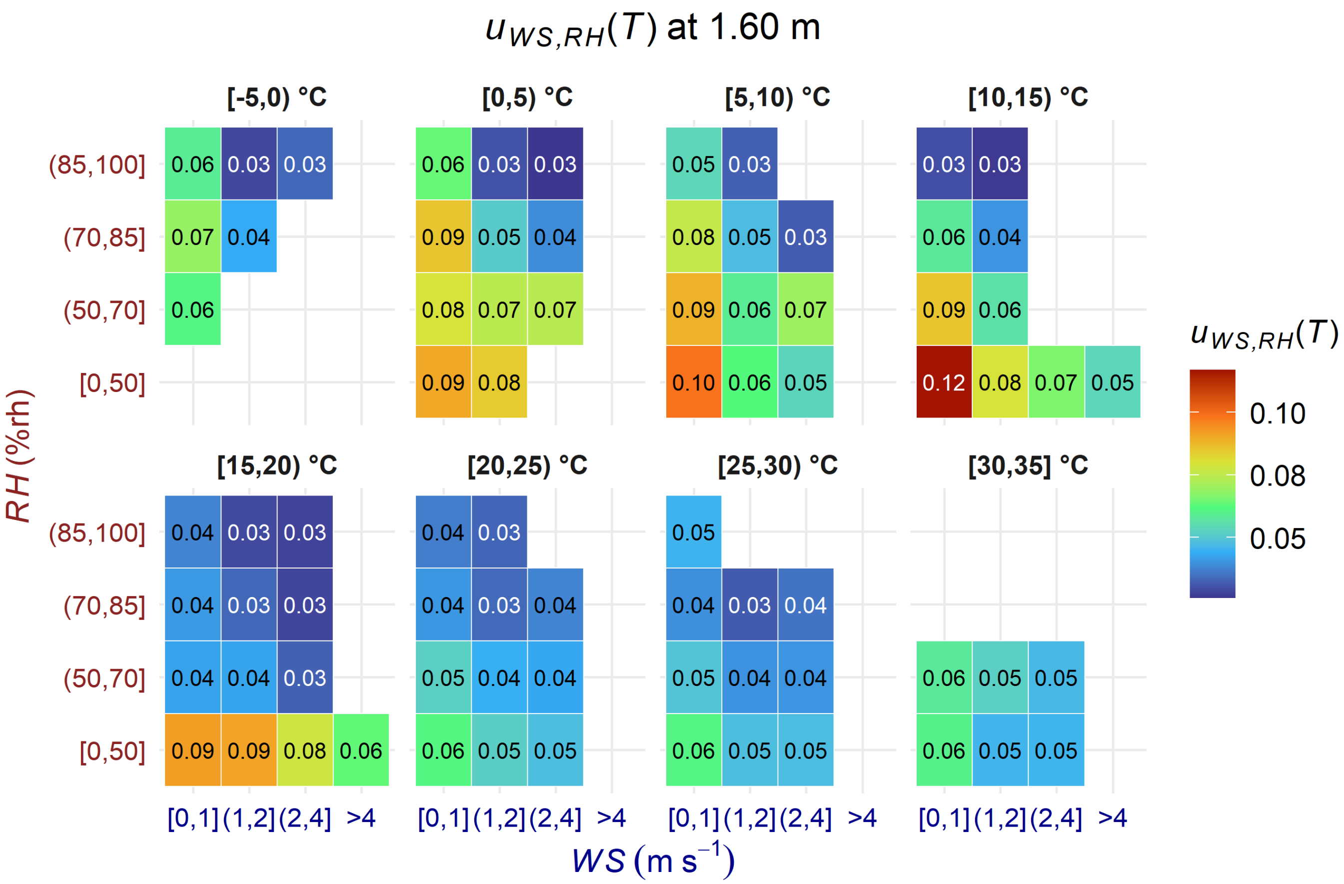

FIGURE 7 | Air temperature uncertainty contribution due to *WS* and *RH*, $u_{WS,RH}(T)$, for the sensor at 1.60 m, evaluated across different combinations of *WS* and *RH* thresholds.

the magnitude of solar irradiance at INRiM. Vallere station, operated and supervised by ARPA Piemonte, is located less than 3 km from the INRiM field and provides quality-controlled meteorological observations. Given their proximity and having similar field characteristics and environments, the global solar radiation measurements in Vallere are considered representative of the experimental zone at INRiM.

Figure 8 shows the daily evolution of a typical summer day in Turin. During the night, ΔT values are predominantly negative, indicating that the sensor at 1.60 m observes temperatures lower than the mean. As the morning progresses and air temperature begins to rise, also the values of ΔT, driven principally by the increase in solar radiation. The dominant winds are lower than 2 m s^{-1} and the dispersion in its measurements is higher between 06:00 and 15:00, coinciding with the highest dispersion of ΔT. According to the theory, after sunrise, heat flux from the ground to the air appears as response to the increase in solar radiation, and it can affect the temperature difference among the thermometers.

Table 3 presents the instantaneous air temperature (T) every 6 h, together with the corresponding *RH* and *WS* values. The uncertainty contributions to the corresponding air temperature measurements are also shown. $u_{syst}(T)$ is 0.02°C, dominated by the calibration contribution; $u_{WS,RH}(T)$ is obtained from Figure 7 and $u_{siting}(T)$ is estimated based on Siting Classifications (WMO 2024a, Annex 1.D). The INRiM field can be categorised in Class 3, which corresponds to a siting standard uncertainty of 1°C. The uncertainty value reported in the WMO guide is general, which means that it may not be fully representative of the siting conditions of the experiment. A conservative approach is here adopted by weighing the WMO suggested value with a rectangular distribution, obtaining in the end $u_{siting}(T) = 0.29$°C. Note that among the uncertainty contributions, $u_{WS,RH}(T)$ is the only one that is not fixed, as it varies according to the environmental conditions.

Figure 9 and Table 4 present the winter study case, characterised by high values of *RH* and *WS* generally below 2 m s^{-1}. These conditions are consistent with the presence of fog, as confirmed by observations at Caselle Station and by the low solar radiation recorded at the Vallere station. Due to fog and high humidity, condensation may form on the screens, leading to increase the temperature differences among the air temperature sensors. As mentioned before, the presence of low *WS* intensifies these differences. Furthermore, in the presence of low incidence of solar radiation, the turbulence by convection is weak, increasing even more the stratification of air temperature near the surface. The peak of the air temperature curve coincides with the maximum value of ΔT and a minimum in *RH*, likely influenced by a slight increase in the incident solar radiation. At noon, the observed air temperature was 0.76°C with $u_{WS,RH}(T) = 0.09$°C.

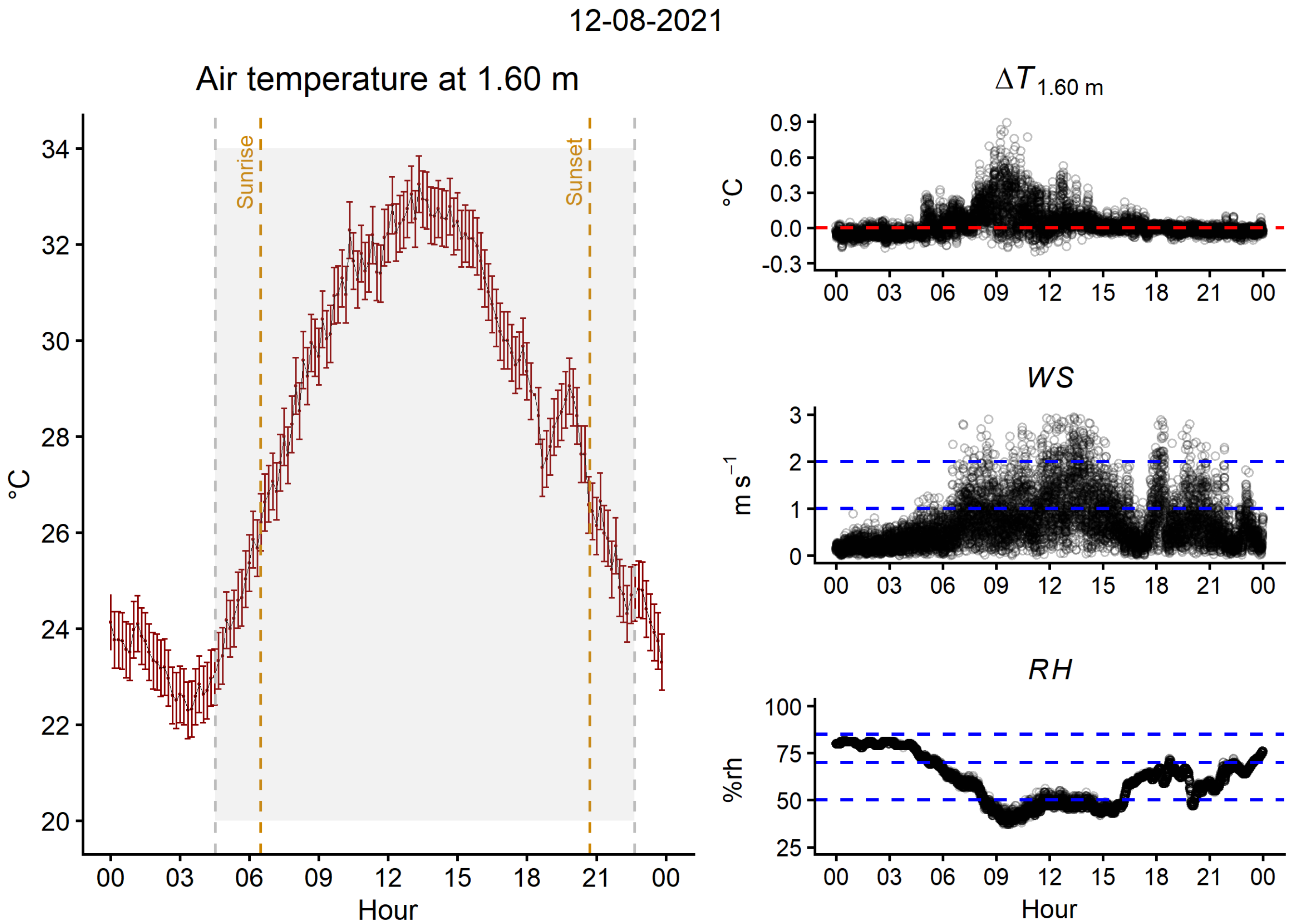

FIGURE 8 | Case study of 12 August 2021. The air temperature is shown with the corresponding expanded uncertainty (red bars), with data every 10 min. The grey shaded area marks the interval between the end and the beginning of the astronomical night, as computed from solar position data. The instantaneous 10-s values of ΔT, *WS* and *RH* are also shown. The red dashed line indicates ΔT equal to 0°C and the blue dashed lines, the thresholds of *WS* and *RH* according to Table 2.

4 | Conclusion

This study investigates how *WS* and *RH* affect air temperature measurements from ground-based stations. For each of the six thermometers installed at two heights (1.60 m and 2.10 m), the air temperature difference is defined as the deviation from the mean temperature and denoted as ΔT. ΔT and the corresponding uncertainty were calculated across 5°C air temperature intervals from −5°C to 35°C. The uncertainty contributions of ΔT are the calibration uncertainty, sensor drift, and the dispersion of the measurements, which represents the highest contribution. Because air temperature measurements were performed under real environmental conditions, the uncertainty of ΔT, calculated for specific ranges of *WS* and *RH*, is interpreted as the air temperature uncertainty due to these variables, denoted as $u_{WS,RH}(T)$. Since the distribution of ΔT depends on sensor height, $u_{WS,RH}(T)$ was evaluated separately for the thermometers installed at 1.60 m and 2.10 m, obtainig values between 0.03°C and 0.12°C.

In line with previous research, this paper highlights the influence of *WS* on air temperature measurements. The presence of calm and low winds strengthens the temperature difference among thermometers. This effect is present even with artificially ventilated radiation shields. It was observed that for *WS* lower than or equal to 2 m s^{-1}, the temperature differences are high, with a higher dispersion of the ΔT distribution. In winter, the temperature differences among the sensors are most pronounced, reaching the median ΔT value of −0.15°C for the sensor at 1.60 m, and 0.09°C for the sensor at 2.10 m. In this period, the percentage of events with high values of *RH* is high, and dew may form. This can generate condensation on the surface of the thermometers, introducing errors in the measurements. ΔT is also affected by solar radiation. The solar heating generates vertical fluxes of air from the ground, warming the air from the bottom to the top. As a consequence, during the day, those thermometers near the ground surface are warmer than those located at the top. During the night, in the absence of this flux, the air remains stratified and the thermometers near the ground are cooler.

This study aims to address the uncertainty evaluation of air temperature measurements under real measurement conditions. For generating climate reference data, it is mandatory to have traceable measurements with a complete analysis of the uncertainty contributions, including the uncertainty due to the environmental conditions. The relevance of the present work lies in the evaluation of $u_{WS,RH}(T)$ for different thermometer

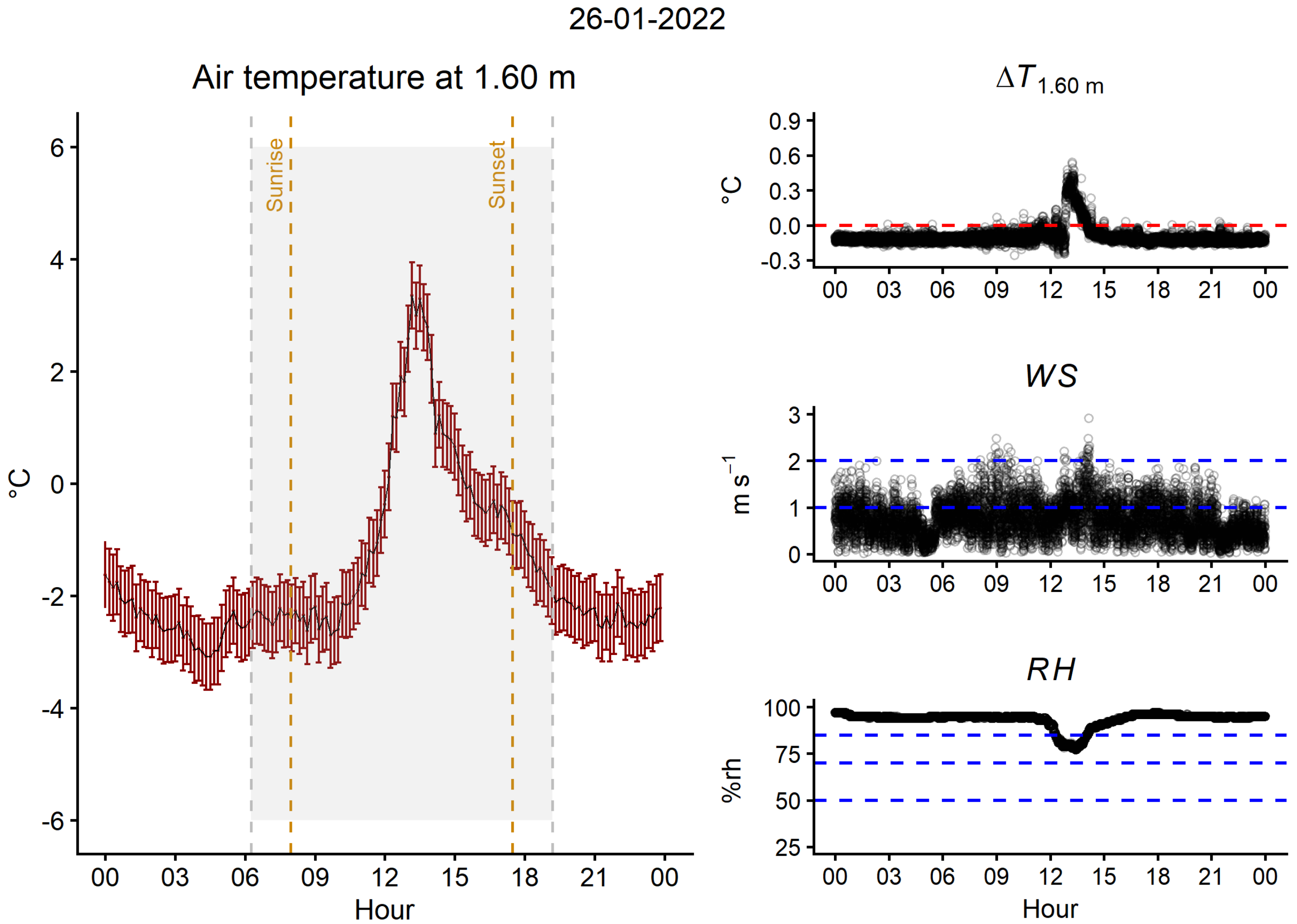

FIGURE 9 | Case study of 26 January 2022. The air temperature is shown with the corresponding expanded uncertainty (red bars), with data every 10 min. The grey shaded area marks the interval between the end and the beginning of the astronomical night, as computed from solar position data. The instantaneous 10-s values of ΔT, *WS* and *RH* are also shown. The red dashed line indicates ΔT equal to 0°C; the blue dashed lines and the thresholds of *WS* and *RH* according to Table 2.

TABLE 3 | Summer case.

Date	T (°C)	WS (m s^{-1})	RH (%rh)	$u_{syst}(T)$ (°C)	$u_{WS,RH}(T)$ (°C)	$u_{siting}(T)$ (°C)	$U(T)$ ($k=2$) (°C)
12-08-2021 00:00	24.15	0.18	80	0.02	0.04	0.29	0.59
12-08-2021 06:00	24.21	0.82	66	0.02	0.05	0.29	0.59
12-08-2021 12:00	32.25	0.20	48	0.02	0.06	0.29	0.59
12-08-2021 18:00	29.29	1.55	64	0.02	0.04	0.29	0.59

Note: Measurements every 6 h of air temperature readings (T) with the associated quantities of influences *WS* and *RH* and the air temperature uncertainty contributions due to the system $u(T_{syst})$, due to *WS* and *RH* $u_{WS,RH}(T)$, and due to the siting $u_{siting}(T)$. The expanded uncertainty with $k=2$ is also presented.

TABLE 4 | Winter case.

Date	T (°C)	WS (m s^{-1})	RH (%rh)	$u_{syst}(T)$ (°C)	$u_{WS,RH}(T)$ (°C)	$u_{siting}(T)$ (°C)	$U(T)$ ($k=2$) (°C)
26-01-2022 00:00	−1.62	0.72	97	0.02	0.06	0.29	0.59
26-01-2022 06:00	−2.44	0.43	95	0.02	0.06	0.29	0.59
26-01-2022 12:00	0.76	1.01	84	0.02	0.09	0.29	0.61
26-01-2022 18:00	−1.06	0.62	97	0.02	0.06	0.29	0.59

Note: Measurements every 6 h of air temperature readings (T) with the associated quantities of influences *WS* and *RH* and the air temperature uncertainty contributions due to the system $u(T_{syst})$, due to *WS* and *RH* $u_{WS,RH}(T)$, and due to the siting $u_{siting}(T)$. The expanded uncertainty with $k=2$ is also presented.

heights and for specific ranges of air temperature. This uncertainty also reflects the influence of physical effects such as condensation and solar heating. The study reveals that winter conditions (−5°C to 15°C) present slightly higher values of $u_{WS,RH}(T)$. Under fog conditions, low temperature values (lower than 5°C) and WS lower than $1\,\mathrm{m\,s^{-1}}$, $u_{WS,RH}(T)$ is 0.06°C for both heights. $u_{WS,RH}(T)$ for similar temperature and wind conditions but RH between 75 and 85%rh, presents higher uncertainty values, ranging between 0.07°C and 0.09°C, depending on sensor height. This behaviour is likely related to the dissipation of radiation fog, where an increase in solar radiation enhances temperature gradients between thermometers, leading to larger measurement dispersion. Overall, the results show a consistent pattern: $u_{WS,RH}(T)$ decreases as WS increases, independently of seasonal conditions and thermometer height. This behaviour reflects the role of wind in enhancing air mixing around the sensors, thereby reducing temperature differences between the thermometer readings.

This analysis allows to include $u_{WS,RH}(T)$ in the uncertainty budget for air temperature measurements from ground-based stations with similar aspirated-shield models, and also associated with sensor height. As shown in the Case Studies section, in addition to the system and siting uncertainties, $u_{WS,RH}(T)$ is considered as an additional source of uncertainty, based on the on-site measurements of WS and RH at the time of the air temperature observations. These uncertainty components are then combined in quadrature and multiplied by a coverage factor $k=2$ to obtain the expanded uncertainty of air temperature under real measurement conditions. For example, on a winter foggy night, a value of $-1.62°\mathrm{C} \pm 0.59°\mathrm{C}$ was observed at the INRiM field by a thermometer at 1.60 m; and on a summer night, $24.15°\mathrm{C} \pm 0.59°\mathrm{C}$. During the day, for instance, $0.76°\mathrm{C} \pm 0.61°\mathrm{C}$ and $32.25°\mathrm{C} \pm 0.59°\mathrm{C}$ for winter and summer, respectively.

The approach proposed in this work is particularly relevant for the climate reference stations, as the uncertainty evaluation is fundamental for the comparability of the data in space and time, and for guaranteeing the reliability of the measurements. To improve the study of the uncertainty budget, the experiment can be repeated, adding sensors to measure the global and absorbed solar radiation, to evaluate locally the influence of solar radiation on air temperature measurements. And for foggy days, a chilled mirror can be used to verify the condensation on solar shields. Future research can include the analysis of precipitation as another quantity of influence. The study also shows the influence of the instrument's height. For a better understanding of this effect, an experiment is running to compare metrologically the measurements associated with different installation heights.

Author Contributions

Graziano Coppa: writing – review and editing, supervision. **Natali Giselle Aranda:** conceptualization, investigation, writing – original draft, methodology, validation, visualization, writing – review and editing, software, formal analysis, data curation. **Chiara Musacchio:** supervision, methodology. **Alberto Bottacin:** writing – review and editing. **Andrea Merlone:** funding acquisition, supervision, conceptualization.

Acknowledgments

The authors thank the Caselle Station and ARPA Piemonte for providing the auxiliary data used in this study. The research was conducted during the PhD Program in Metrology at the Polytechnic of Turin. The PhD Program received financial support from PON REACT-EU 2014-2020—action IV.5 "PhD programmes on green topic", according to the Ministerial Decree of 10 August 2021, no. 1061. Open access publishing facilitated by Istituto Nazionale di Ricerca Metrologica, as part of the Wiley - CRUI-CARE agreement.

Conflicts of Interest

The authors declare no conflicts of interest.

Data Availability Statement

The data that support the findings of this study are available from the corresponding author upon reasonable request.

References

Ashkenazy, Y., and H. Yizhaq. 2023. "The Diurnal Cycle and Temporal Trends of Surface Winds." *Earth and Planetary Science Letters* 601: 117907. https://doi.org/10.1016/j.epsl.2022.117907.

Best, A. C. 1953. "The Relative Humidity in Radiation Fog." *Tellus* 5, no. 1: 32–35. https://doi.org/10.3402/tellusa.v5i1.8565.

Bojinski, S., M. Verstraete, T. C. Peterson, C. Richter, A. Simmons, and M. Zemp. 2014. "The Concept of Essential Climate Variables in Support of Climate Research, Applications, and Policy." *Bulletin of the American Meteorological Society* 95, no. 9: 1431–1443. https://doi.org/10.1175/BAMS-D-13-00047.1.

Burt, S., and M. de Podesta. 2020. "Response Times of Meteorological Air Temperature Sensors." *Quarterly Journal of the Royal Meteorological Society* 146, no. 731: 2789–2800. https://doi.org/10.1002/qj.3817.

Cassardo, C., R. Forza, M. Manfrin, et al. 2002. "The Urban Meteorological Station of Turin." 311–320. https://iris.unito.it/handle/2318/19083.

Çengal, Y. A., and A. J. Ghajar. 2015. *Heat and Mass Transfer Fundamentals & Applications*. 5th ed. Grawhil Education.

Coppa, G., C. Musacchio, F. Becherini, M. Mazzola, A. Viola, and A. Merlone. 2024. "On-Site Calibration of Instruments in the Arctic: Assessment of Temperature Records at Climate Change Tower in Ny-Ålesund, Svalbard." *Arctic Science* 10, no. 4: 643–652. https://doi.org/10.1139/as-2024-0008.

Coppa, G., A. Quarello, G.-J. Steeneveld, N. Jandrić, and A. Merlone. 2021. "Metrological Evaluation of the Effect of the Presence of a Road on Near-Surface Air Temperatures." *International Journal of Climatology* 41: 3705–3724. https://doi.org/10.1002/joc.7044.

Dahl, E. O., K.-E. Frøysa, and P. Lunde. 2003. *Handbook of Uncertainty Calculations. Fiscal Orifice Gas and Turbine Oil Metering Stations*, 220. Handbook Prepared on Behalf of the Norwegian Society for Oil and Gas Measurement (NFOGM), Norwegian Petroleum Directorate (NPD) and the Norwegian Society of Chartered Engineers (NIF).

Dai, A. 2023. "The Diurnal Cycle From Observations and ERA5 in Surface Pressure, Temperature, Humidity, and Winds." *Climate Dynamics* 61: 2965–2990. https://doi.org/10.1007/s00382-023-06721-x.

de Podesta, M., S. Bell, and R. Underwood. 2018. "Air Temperature Sensors: Dependence of Radiative Errors on Sensor Diameter in Precision Metrology and Meteorology." *Metrologia* 55, no. 2: 229–244. https://doi.org/10.1088/1681-7575/aaaa52.

Erell, E., V. Leal, and E. Maldonado. 2005. "Measurement of Air Temperature in the Presence of a Large Radiant Flux: An Assessment of Passively Ventilated Thermometer Screens." *Boundary-Layer Meteorology* 114: 205–231. https://doi.org/10.1007/s10546-004-8946-8.

Fajber, R., A. H. Monahan, and W. J. Merryfield. 2014. "At What Time of Day Do Daily Extreme Near-Surface Wind Speeds Occur?" *Journal of Climate* 27, no. 11: 4226–4244.

Fratianni, S., C. Cassardo, and R. Cremonin. 2009. "Climatic Characterization of Foehn Episodes in Piedmont, Italy." *Geografia Fisica e Dinamica Quaternaria* 32, no. 1: 15–22. https://iris.unito.it/handle/2318/75947?mode=simple.

Garcia Izquierdo, C., G. Coppa, S. Hernández, and A. Merlone. 2024. "Metrological Evaluation of the Building Influence on Air Temperature Measurements." *Atmosphere* 15, no. 2: 209. https://doi.org/10.3390/atmos15020209.

Garratt, J. R. 1992. *The Atmospheric Boundary Layer*. Cambridge University Press.

Geiger, R., R. H. Aron, and P. Todhunter. 2009. *The Climate Near the Ground*. Rowman & Littlefield. https://doi.org/10.1007/978-3-322-86582-3.

Global Climate Observing System (GCOS). 2021. *GCOS Surface Reference Network (GSRN): Justification, Requirements, Siting and Instrumentation Options (GCOS Report No. 226)*. World Meteorological Organization. https://library.wmo.int/idurl/4/56671.

Harrison, R. G. 2010. "Natural Ventilation Effects on Temperatures Within Stevenson Screens." *Quarterly Journal of the Royal Meteorological Society* 136: 253–259. https://doi.org/10.1002/qj.537.

Harrison, R. G. 2015. *Meteorological Measurements and Instrumentation*. John Wiley & Sons.

Harrison, R. G., and S. D. Burt. 2021. "Quantifying Uncertainties in Climate Data: Measurement Limitations of Naturally Ventilated Thermometer Screens." *Environmental Research Communications* 3, no. 6: 061005. https://doi.org/10.1088/2515-7620/ac0d0b.

He, Y., A. H. Monahan, and N. A. McFarlane. 2013. "Diurnal Variations of Land Surface Wind Speed Probability Distributions Under Clear-Sky and Low-Cloud Conditions." *Geophysical Research Letters* 40, no. 12: 3308–3314. https://doi.org/10.1002/grl.50575.

JCGM. 2008. "Evaluation of Measurement Data Guide to the Expression of Uncertainty in Measurements. GUM 1995 With Minor Corrections." https://doi.org/10.59161/JCGM100-2008E.

JCGM. 2012. "The International Vocabulary of Metrology—Basic and General Concepts and Associated Terms (VIM), Volume 200." https://doi.org/10.59161/JCGM200-2012.

Lanzante, J. R. 1996. "Resistant, Robust and Non-Parametric Techniques for the Analysis of Climate Data: Theory and Examples, Including Applications to Historical Radiosonde Station Data." *International Journal of Climatology* 16, no. 11: 1197–1226. https://doi.org/10.1002/(SICI)1097-0088(199611)16:11<1197::AID-JOC89>3.0.CO;2-L.

Lin, X., K. G. Hubbard, E. A. Walter-Shea, J. R. Brandle, and G. E. Meyer. 2001. "Some Perspectives on Recent In Situ Air Temperature Observations: Modeling the Microclimate Inside the Radiation Shields." *Journal of Atmospheric and Oceanic Technology* 18, no. 9: 1470–1484. https://doi.org/10.1175/1520-0426(2001)018<1470:SPORIS>2.0.CO;2.

Liu, W., Y. Han, J. Li, X. Tian, and Y. Liu. 2018. "Factors Affecting Relative Humidity and Its Relationship With the Long-Term Variation of Fog-Haze Events in the Yangtze River Delta." *Atmospheric Environment* 193: 242–250. https://doi.org/10.1016/j.atmosenv.2018.09.015.

Mahrt, L. 1998. "Stratified Atmospheric Boundary Layers." *Boundary-Layer Meteorology* 90, no. 3: 375–396. https://doi.org/10.1023/A:1001765727956.

Markowski, P., and Y. Richardson. 2011. *Mesoscale Meteorology in Midlatitudes*. John Wiley and Sons.

Mauder, M., R. L. Desjardins, Z. Gao, and R. van Haarlem. 2008. "Errors of Naturally Ventilated Air Temperature Measurements in a Spatial Observation Network." *Journal of Atmospheric and Oceanic Technology* 25, no. 11: 2145–2151. https://doi.org/10.1175/2008JTECHA1046.1.

Merlone, A., H. Al-Dashti, N. Faisal, et al. 2019. "Temperature Extreme Records: World Meteorological Organization Metrological and Meteorological Evaluation of the 54.0°C Observations in Mitribah, Kuwait and Turbat, Pakistan in 2016/2017." *International Journal of Climatology* 39: 5154–5169. https://doi.org/10.1002/joc.6132.

Merlone, A., G. Beges, A. Bottacin, et al. 2024. "Climatological Reference Stations: Definitions and Requirements." *International Journal of Climatology* 44, no. 5: 1710–1724. https://doi.org/10.1002/joc.8406.

Musacchio, C., G. Coppa, G. Begeš, et al. 2021. "Effect of Snow-Covered Ground Albedo on the Accuracy of Air Temperature Measurements." *Atmospheric Measurement Techniques* 14, no. 9: 6195–6212. https://doi.org/10.5194/amt-14-6195-2021.

Musacchio, C., G. Coppa, and A. Merlone. 2019. "An Experimental Method for Evaluation of the Snow Albedo Effect on Near-Surface Air Temperature Measurements." *Meteorological Applications* 26: 161–170. https://doi.org/10.1002/met.1756.

Nakamura, R., and L. Mahrt. 2005. "Air Temperature Measurement Errors in Naturally Ventilated Radiation Shields." *Journal of Atmospheric and Oceanic Technology* 22, no. 7: 1046–1058. https://doi.org/10.1175/JTECH1762.1.

Nielsen, J., A. Bottacin, P. Østergaard, et al. 2024. "Evaluation of the Influence of Rain on Air Surface Temperature Measurements." *Measurement Science and Technology* 36, no. 2: 025801. https://doi.org/10.1088/1361-6501/ada1ea.

Richardson, S. J., F. V. Brock, S. R. Semmer, and C. Jirak. 1999. "Minimizing Errors Associated With Multiplate Radiation Shields." *Journal of Atmospheric and Oceanic Technology* 16, no. 11: 1862–1872. https://doi.org/10.1175/1520-0426(1999)016<1862:MEAWMR>2.0.CO;2.

Stull, R. B. 2012. *An Introduction to Boundary Layer Meteorology*. Vol. 13. Springer Science & Business Media.

Thorne, P. W., M. J. Menne, C. N. Williams, et al. 2016. "Reassessing Changes in Diurnal Temperature Range: A New Data Set and Characterization of Data Biases." *Journal of Geophysical Research: Atmospheres* 121: 5115–5137. https://doi.org/10.1002/2015JD024583.

Van de Wiel, B. J. H., E. Vignon, P. Baas, et al. 2017. "Regime Transitions in Near-Surface Temperature Inversions: A Conceptual Model." *Journal of the Atmospheric Sciences* 74, no. 4: 1057–1073. https://doi.org/10.1175/JAS-D-16-0180.1.

WMO. 1981. *Lecture Notes for Training Class II and Class III Agricultural Meteorological Personnel (WMO-No. 551)*. WMO. https://library.wmo.int/idurl/4/31139.

WMO. 2010a. *Implementation Plan for the Global Observing System for Climate in Support of the UNFCCC, GCOS-138*. World Meteorological Organization. https://library.wmo.int/idurl/4/58703.

WMO. 2010b. *Guideline for the Generation of Datasets and Products Meeting GCOS Requirements, GCOS-143*. World Meteorological Organization. https://library.wmo.int/idurl/4/39563.

WMO. 2024a. "Guide to Instruments and Methods of Observation." WMO-No. 8, Volume I. https://library.wmo.int/idurl/4/68695.

WMO. 2024b. "Manual on the WMO Integrated Global Observing System." (WMO-No. 1160). https://library.wmo.int/idurl/4/55063.

WMO. 2025. *The 2022 GCOS ECVs Requirements*. Vol. 245. World Meteorological Organization. https://library.wmo.int/idurl/4/58111.

Woolliams, E., M. Cox, X. Loizeau, et al. 2025. "A Metrological Framework for Addressing Uncertainty in Satellite and In Situ Earth Environmental Observations." *Surveys in Geophysics*. https://doi.org/10.1007/s10712-025-09916-5.